A Bayesian Structural Time Series Approach for Predicting Red Sea Temperatures

Nabila Bounceur, Ibrahim Hoteit, and Omar Knio

***Abstract*—Sea surface temperature (SST) is a leading factor impacting coral reefs and causing bleaching events in the Red Sea. A long-term prediction of temperature patterns with an estimate of uncertainty is thus essential for environment management of the Red Sea ecosystem. In this work, we build a data-driven Bayesian structural time series model and show its effectiveness in predicting future SST seasons with a high accuracy, and identifying the main predictive factors of future SST variability among a large number of factors, including regional SST and large-scale climate indices. The modeling scheme proposed here applies an efficient hierarchical clustering to identify interconnected subregions that display distinct SST variability over the Red Sea, and a Markov Chain Monte Carlo algorithm to simultaneously select the main predictors while the time series model is being trained. In particular, numerical results indicate that monthly SST can be reliably predicted for five months ahead.**

***Index Terms*—Bayesian structural time series (BSTS), factor selection, hierarchical clustering, Markov chain Monte Carlo (MCMC), predictive modeling, red sea, sea surface temperature (SST).**

I. Introduction

RED Sea coral reefs are experiencing bleaching, the most problematic change that may have happened to this ecosystem [1]–[3]. Bleaching events are believed to be significantly influenced, at a first level, by thermal stress from sea surface temperature (SST) [4]. Consequently, any decision making related to management strategies of Red Sea ecosystem must rely on SST predictions.

The Red Sea (see Fig. 1) is located in an area that lies in a transitional region with potential influence from the Atlantic, Indian Ocean, and Pacific Ocean [5]. Accordingly, SST predictions must incorporate, in addition to information accounting for its past spatiotemporal variability, potential global, and regional predictors, such as the El Niño Southern Oscillation (ENSO), the North Atlantic Oscillation (NAO), and the Arctic Oscillation (AO) (e.g., [6]–[10]).

Manuscript received May 17, 2019; revised February 6, 2020 and March 13, 2020; accepted March 31, 2020. Date of publication April 23, 2020; date of current version May 21, 2020. This work was supported by the Office of Sponsored Research, King Abdullah University of Science and Technology through the "Virtual Red Sea Initiative" under Grant REP/1/3268–01–01. *(Corresponding author: Nabila Bounceur.)*

Nabila Bounceur and Omar Knio are with the Division of Computer, Electrical and Mathematical Science and Engineering, King Abdullah University of Science and Technology, Thuwal 23955, Saudi Arabia (e-mail: nabila.bounceur@kaust.edu.sa; omar.knio@kaust.edu.sa).

Ibrahim Hoteit is with the Department of Physical Sciences and Engineering, King Abdullah University of Science and Technology, Thuwal 23955, Saudi Arabia (e-mail: ibrahim.hoteit@kaust.edu.sa).

Digital Object Identifier 10.1109/JSTARS.2020.2989218

Seasonal predictability of SST to a set of predictors may be achieved by using climate simulators [11]. Long-term predictions with general climate models (GCMs) is, however, challenging. This is due to fundamental limitations arising from predictability limits (see, e.g., [12], [13] for seasonal climate forecasts reliability). Specifically, the application of GCMs proved challenging for SST predictions over the tropics [14].

Many approaches to improve SST prediction are based on superensemble models developed by combining a large ensemble of coupled ocean-atmosphere models or by using multimodel prediction systems [15]. This requires additional analysis of the ensembles to adequately construct the combined model, in addition to statistical correction methods to improve seasonal prediction needed for most GCMs.

The most relevant application of a dynamical–statistical correction method to obtain improved predictions can be found in the recent study of Hong *et al.*[16], who predicted the main modes of SST over the equatorial eastern Pacific. In this study, handful *a priori* climate indices were used that were selected, and no time lags were included in the predictors.

When the set of predictors is large and a systematic selection is required, previous approaches may become infeasible for long-term predictions, as a large number of experiments should be designed and run. Statistical methodologies emerged as an alternative means of climate forecasting. Previous attempts linked SST statistically to its past spatiotemporal values only, using among others, canonical correlation analysis [17], singular spectral analysis [18], and neural networks [19]. See, for e.g., Mason and Mimmack [20] for a comparative study.

Although previous investigations considered the associations between indices of climate variability and SST (e.g., [21]–[23]), few were applied over the Red Sea (e.g., [24]–[26]). Moreover, these studies considered single, or a small set of these climate indices, which were selected *a priori*. The selection was mainly based on a correlation analysis between the time series of the climate indices and of the SST time series, or by applying *a priori* knowledge of an association due to the physics of the climate system. See, for instance, the study of Xue *et al.* [27], who used wind stress and sea-level indices as predictors of east Pacific SST.

Several statistical methods may be applied to estimate the time lag in potential predictors, including partial autocorrelation function, ensemble empirical mode decomposition, and cross-correlation analysis (e.g., [28]). These methods are applied *a priori* and do not take into account the impact of the selection on the predictive ability of SST model in a systematic way. Pseudo

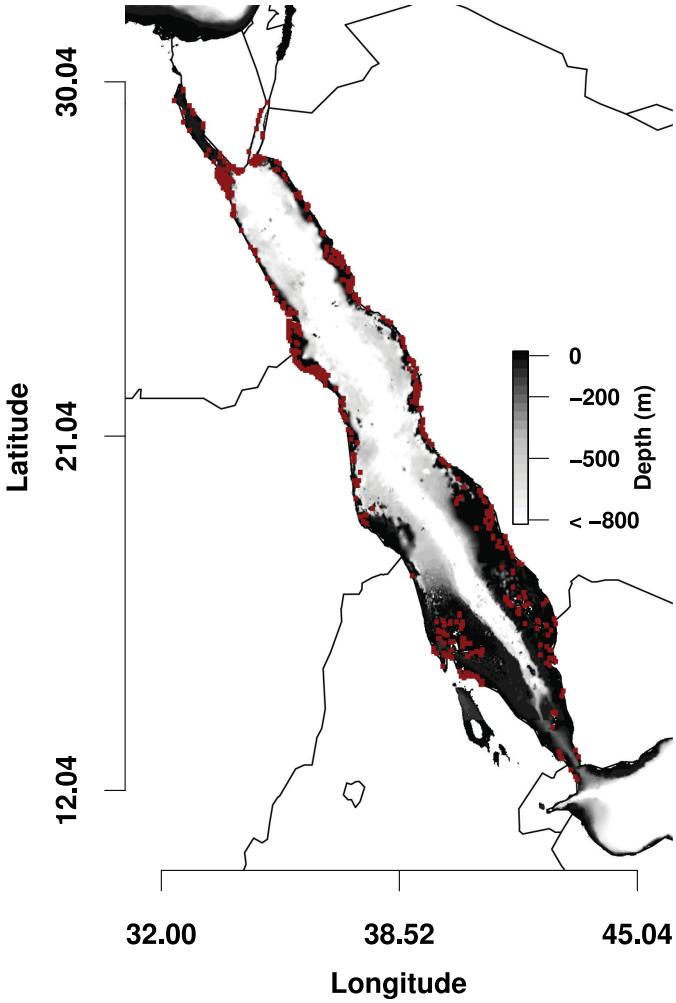

Fig. 1. Longitude–latitude map showing the Red Sea and its coral reef locations. The Red Sea extends from 12.5°N to 30°N (about $\sim 2500\,\mathrm{km}$ in length) and from 31°E to 46°E (maximum width of $\sim 300\,\mathrm{km}$). The bathymetry of the Red Sea is shown in grey colors. Depths between 0 and $-200\,\mathrm{m}$ are emphasized in dark grey; main coral reef locations are indicated by red dots. Data of elevations (m) relative to the sea are extracted from "The GEBCO One Minute Grid dataset" (http://www.gebco.net/data_and_products/gridded_bathymetry_data/). The coral reefs locations dataset is extracted from the comprehensive global dataset of warm-water coral reefs (tropical and subtropical regions) (http://data.unep-wcmc.org/datasets/1).

Bayes factor [29] may also be used for predictors' selection, as a measure of the statistical evidence supporting the use of lagged climate indices (see, e.g., [30]). However, it relies on variations of one predictor at a time while testing the predictive ability of the system, which can be appealing for large set of predictors.

This work aims at investigating the seasonal predictability of SST in the Red Sea using a data-driven approach, while simultaneously selecting relevant predictors and estimating modeling uncertainties.

Here, we apply a Bayesian structural time series (BSTS) framework that incorporates a clustering approach to identify interconnected subregions that display distinct SST variability over the Red Sea, and a Markov chain Monte Carlo (MCMC) algorithm to simultaneously select the main predictors while the model is being trained over each cluster.

The framework views the Red Sea as a black-box system, with past SST and climate indices as inputs, and future SST as output. In this context, we apply a BSTS model [31], [32], a well-established machinery, to assess the long-term predictability of SST in the Red Sea, based on observations and large-scale climate indices. This includes a systematic selection of the predictors and the relative time lags. Moreover, in this framework, predictions are made over SST clusters identified based on the similarity of their long-term variability by using a hierarchical clustering technique.

To the best of our knowledge, this is the first study that analyzes, in a systematic way, the relationship between all global climate indices and SST variability in the Red Sea, and uses a Bayesian model to make predictions over regions exhibiting similar dynamics.

The rest of this article is organized as follows. Section II is devoted to climate data description and Section III presents the modeling framework, including the data processing and analysis. Results are provided in Section IV, which also includes a discussion of the selection of SST predictors, the validity of the SST representation, and the future seasonal predictions. Main conclusions are provided in Section V.

II. Data Description

We considered monthly mean SST over the Red Sea (see Fig. 1) provided by the European Centre for Medium-Range Weather Forecasts Interim (ERA-Interim) reanalysis from 1979 to 2016 [33], [34]. We also considered the historical observed monthly time series covering the period 1979–2016 of seven climate indices.

These include ENSO[35], [36], AO [9], [37], NAO [38], [39], Dipole Mode Index (DMI) [40], Madden–Julian Oscillation (MJO) [41], East Atlantic–Western Russia pattern (EAWR) [42], [43], and Pacific Decadal Oscillation (PDO) [44]. The records were obtained from the online archives of the National Centre for Atmospheric Research and the National Oceanic and Atmospheric Administration.

ENSO is the most important driver of interannual climate variability near the equatorial Pacific Ocean and it affects the climate in large parts of the world (e.g., [45], [46]). The data considered here are the multivariate ENSO index (MEI). MEI reflects the nature of the coupled ocean-atmosphere system.

AO is an index of the dominant large-scale pattern of nonseasonal sea-level pressure variations north of 20°N between the midlatitudes and Arctic atmospheric mass.

NAO is a prominent mode of atmospheric variation over the North Atlantic in all seasons and surrounding regions [47].

DMI is an index of anomalous SST gradient between the western equatorial Indian Ocean and the South Eastern equatorial Indian Ocean.

The MJO is a tropical disturbance that occurs mainly in the Indian Ocean and the Pacific Ocean. It has wide ranging impacts on the patterns of tropical and extratropical surface temperature around the global tropics and subtropics. The MJO informs where convection is active in the tropics, and was shown to influence the intensity ENSO cycle [48].

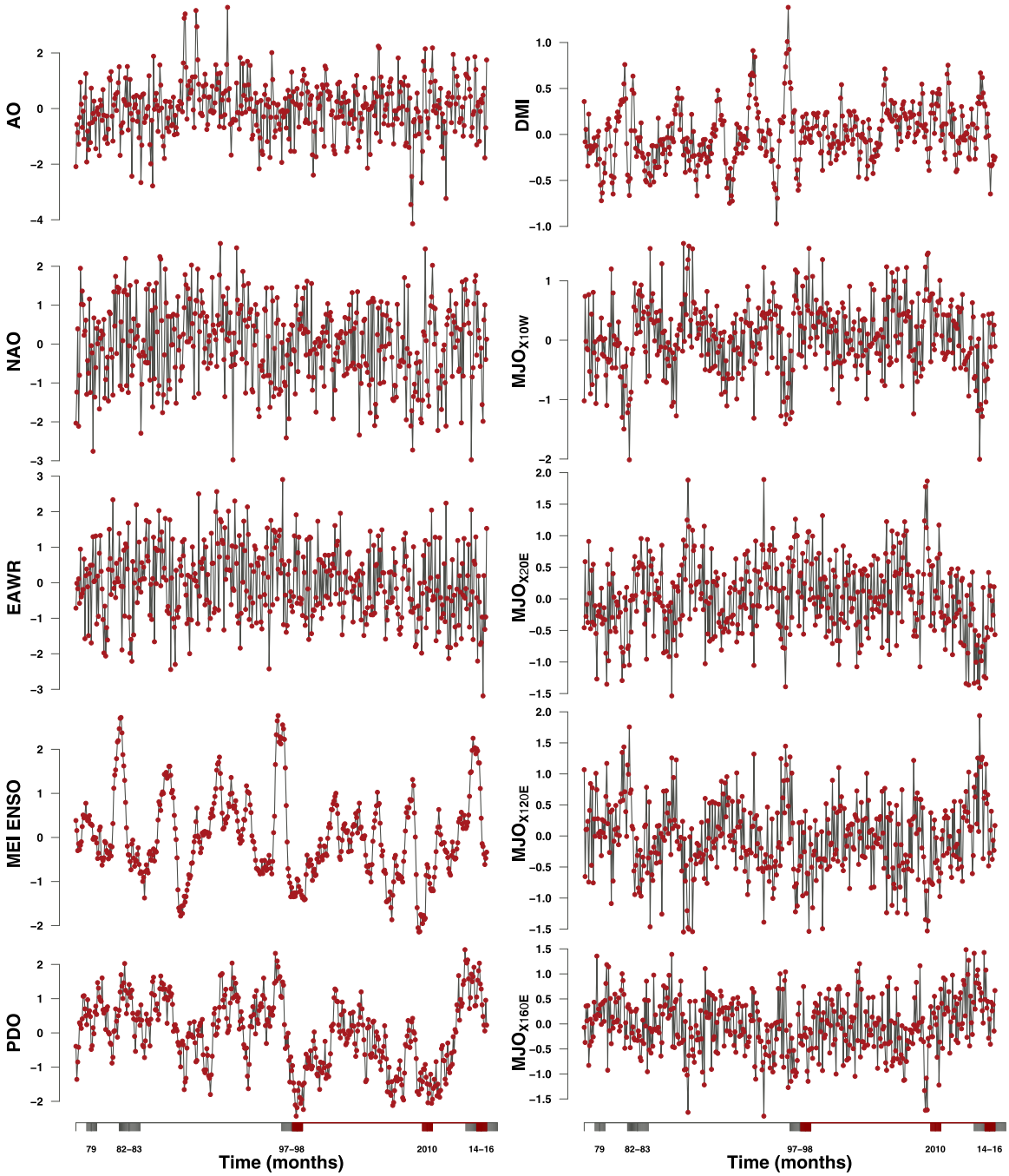

Fig. 2. Time series of monthly climate indices from January 1978 to September 2018. Plotted are curves for AO, NAO, EAWR, ENSO, PDO, DMI, and MJO (20°E, 120°E, 160°E, 120°W, 10°W), as indicated.

EAWR describes the teleconnection patterns with an important component in the North Atlantic region. These patterns affect Eurasia during most of the year and they are related to the planetary Rossby wave energy propagation with several anomaly centers ranging from the Caspian Sea to Newfoundland [43]. This mode tends to be weak through Middle East. The PDO index is the leading mode of monthly SST anomalies (SSTA) in the North Pacific Ocean, poleward of 20°N. It resembles ENSO but at a decadal scale.

The corresponding time series of some of the climate indices are illustrated in Fig. 2. The curves show that the climate indices exhibit high variability. Table I provides the corresponding summary statistics.

III. Modeling Framework

The modeling framework is schematically illustrated in Fig. 3. It consists in a BSTS model that incorporates a hierarchical

TABLE I
QUANTILES OF THE CLIMATE INDICES VALUES OVER THE TIME PERIOD 1979–2016

Quantiles	AO	NAO	EAWR	PDO	DMI	MEI ENSO
0%	-4.266	-3.14	-2.46	-2.33	-0.905	-1.892
25%	-0.558	-0.705	-0.775	-0.465	-0.186	-0.286
50%	-0.015	0.08	-0.03	0.35	0.038	0.309
75%	0.579	0.76	0.65	1.03	0.296	0.912
100%	3.495	3.06	2.72	3.51	1.661	3.008

	MJO modes									
Quantiles	**X160E**	**X140E**	**X120E**	**X100E**	**X80E**	**X70E**	**X20E**	**X10W**	**X40W**	**X120W**
0%	-1.478	-1.398	-1.462	-1.717	-1.569	-1.734	-1.888	-1.818	-2.017	-2.025
25%	-0.377	-0.364	-0.431	-0.457	-0.437	-0.448	-0.369	-0.306	-0.275	-0.303
50%	0.024	-0.029	-0.033	-0.064	-0.023	-0.058	-0.038	0.053	0.066	0.065
75%	0.413	0.323	0.309	0.269	0.337	0.322	0.349	0.374	0.441	0.449
100%	1.912	1.702	1.78	2.013	1.812	1.775	1.462	1.436	1.687	1.596

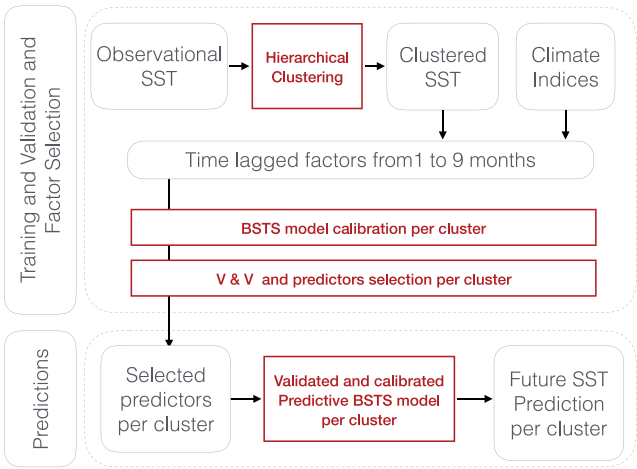

Fig. 3. Flowchart summarizing the proposed methodology. The BSTS model combines three main methods: Kalman filter to estimate the structural model parameters, including trend and seasonality; a spike and slab regression to predict with selected predictors; and Bayesian model averaging to estimate the best performing prediction model with an estimate of uncertainty.

clustering approach, and an MCMC algorithm to objectively select main predictors while the model is being trained.

A. Data Clustering

To assess the relationship between SST over the Red Sea and the different large-scale climate variability indices, we first identified interconnected subregions that display distinct SST variability over the Red Sea and then find links between them and climate indices. The subdivisions are obtained by means of a hierarchical clustering approach [49] applied to the acquired monthly SSTA time series.

Hierarchical clustering is based on the agglomerative scheme to merge the time series into distinct clusters. Initially, each time series is assigned to its own cluster. The clustering algorithm iteratively merges two most similar clusters, and the process is repeated until similar time series can no longer be identified and a single cluster is consequently formed. The clusters to be merged are chosen such that the increase in inner variability (the sum of the squared Euclidean distance matrix of pairwise dissimilarities) of the resulting cluster is minimal (Ward' s minimum variance criterion [50]).

TABLE II
AGGLOMERATIVE COEFFICIENT (AGG. COEF.) MEASURING THE AMOUNT OF CLUSTERING STRUCTURE ESTIMATED FOR DIFFERENT LINKAGE METHODS

Linkage	Description	Agg. coef.
Mean or Average	Average of the dissimilarities between the points in one cluster and the points in an other cluster.	0.9806
Minimum or Single	Smallest dissimilarity between a point in one cluster and a point in an other cluster	0.9563
Maximum or Complete	Largest dissimilarity between a point in one cluster and a point in an other cluster	0.9871
Ward's minimum variance	Minimizes the total within-cluster variance	0.9991

Note: The selected linkage method corresponds to the highest agglomerative coefficient.

Ward's minimum variance merging criteria are selected after assessing its agglomerative coefficient that has the highest value among the main linkage methods (see Table II).

The relevant number of clusters corresponds to the optimal score of a set of 15 quality indices proposed in the literature [51]. These indices determine how well each time series lies within its cluster.

A concise description of quality criteria used to select the optimal number of clusters using a hierarchical clustering based on Ward's minimum variance merging method is summarized in Table III. According to the majority rule, we identified three interconnected subregions of SSTA shown in Fig. 4.

Characteristics of SST and SSTA of each region are summarized in Table IV and the corresponding time series are superimposed on Fig. 5.

B. BSTS Model

We consider a BSTS model per clustered region to predict monthly mean SSTA, denoted herein y_t. Thanks to the modularity and flexibility of structural models [31], the predictive model is expressed as a superimposition of a time series component, where the general trend (μ_t) and the seasonal patterns (ξ_t) in

TABLE III
LIST AND DESCRIPTION OF THE STATISTICAL INDICES USED TO SELECT THE OPTIMAL NUMBER OF CLUSTERS AFTER APPLYING A HIERARCHICAL CLUSTERING BASED ON WARD'S MINIMUM VARIANCE LINKAGE METHOD

Index	Concise description	Reference	Optimal value	
K L	expression based on the within-group dispersion matrix for clustered data	Krzanowski and Lai [69]	Maximum value of the index	3
C H	expression based on the between-group dispersion matrix for clustered data	Calinski and Harabasz [70]	Maximum value of the index	3
Hartigan	expression based on the within-group dispersion matrix for clustered data	Hartigan [71]	Maximum difference between hierarchy levels of the index	3
Cindex	expression based on the smallest and the largest smallest distances between all the pairs of points in the entire data set	Hubert and Levin [72]	Minimum value of the index	10
D B	expression based on the sum ratio of within-cluster scatter to between-cluster separation	Davies and Bouldin [73]	Minimum value of the index	3
Silhouette	based on the distance between a data and a cluster	Rousseeuw [74]	Maximum value of the index	3
Ptbiserial	point biserial correlation coefficient estimated between the raw input dissimilarity matrix and a corresponding matrix consisting of 0 or 1 entries	Milligan [75], [76]	Maximum value of the index	3
Gap	gap statistic	Tibshirani et al. [77]	Minimum value of the index	2
Frey	ratio of difference scores from two successive levels in the hierarchy.	Frey and Van Groenewoud [78]	The cluster level before the index value fell below 1	1
McClain	ratio expression based on the average within and between cluster distances	Rohlf [79] , Milligan [76]	Minimum value of the index	2
Dunn	expression based on the distance between clusters and the diameter of the clusters	Dunn [80]	Maximum value of the index	4
S D	expression based on the concepts of average scattering for clusters and total separation between clusters	Halkidi et al. [81]	Minimum value of the index	3
S Dbw	expression based on the criteria of compactness and separation between clusters	Halkidi and Vazirgiannis [82]	Minimum value of the index	10
Ratkowsky	expression based on the average of ratios depending on the sum of squares between the clusters	Ratkowsky and Lance [83]	Maximum value of the index	3
Ball	expression based on the average distance of the data to their respective cluster centroids	Ball and Hall [84]	Maximum difference between hierarchy levels of the index	3

Note: Optimal number of clusters is identified according to the majority rule, fixed to three clusters.

TABLE IV
STATISTICS OF SST AND SSTA IN INDIVIDUAL REGIONS

Region	Grid points	Variable	Summary statistics (°C)						
			mean	sd	Median	Q1	Q2	min	max
1	521	SST	29.15	2.33	29.40	26.74	31.42	25.29	32.83
		SST Anomaly	0		0.26	-2.41	2.27	-3.86	3.68
2	963	SST	29.01	1.96	29.51	27.15	30.81	24.78	32.20
		SST Anomaly	0		0.50	-1.86	1.80	-4.23	3.20
3	947	SST	26.54	2.4	26.67	24.30	28.68	22.01	30.89
		SST Anomaly	0		0.14	-2.24	2.14	-4.53	4.35

Note: The monthly data for the time period 1979–2016 (456 time steps) was used to obtain the estimates provided. $Q1$ and $Q2$ are the main quantiles.

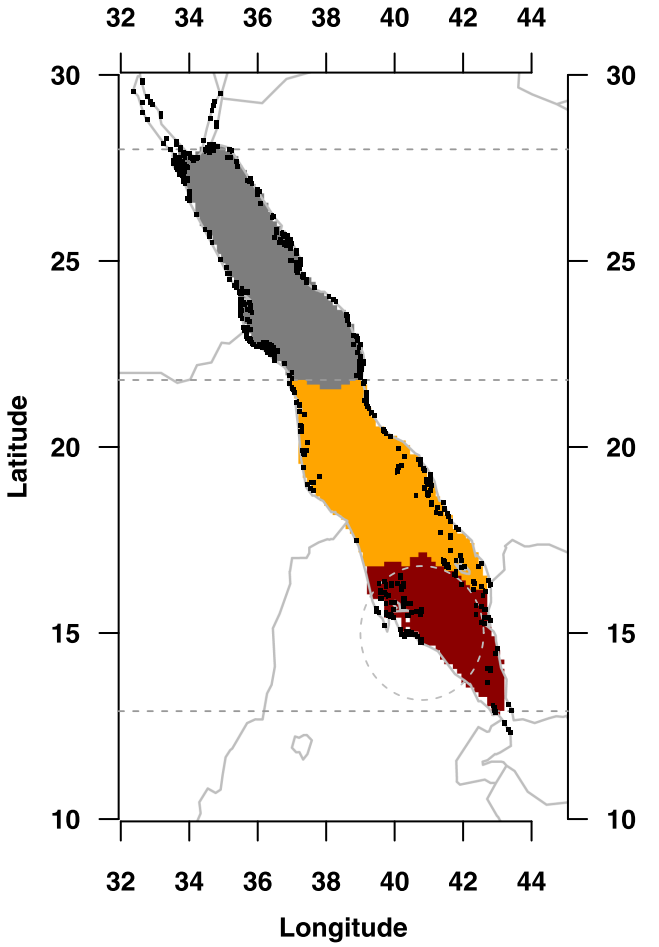

Fig. 4. Longitude–latitude map showing three clustered regions of SSTA over the Red Sea. The Southern Red Sea [SRS, Region 1, between 12.9°N and the dashed circle (40.8°N, 15°N, 1.8)] is depicted in dark red, the Central Red Sea (CRS, Region 2, between limits of the circle and 21.8°N) in orange, and the Northern Red Sea (NRS, Region 3, between 21.8°N and 28°N) in grey.

the data are captured, and a regression component where the contribution of the climate indices (predictors, denoted as $\mathbf{x}_t$) is incorporated. This model is formulated as follows:

$$
\begin{aligned}
y_{t+1} &= \mu_t + \xi_t + \beta^T \mathbf{x}_t + V_y \\
\mu_{t+1} &= \mu_t + \delta_t + V_\mu \\
\delta_{t+1} &= \begin{cases} \delta_t + V_\delta \\ \text{or} \\ D + \rho\,(\delta_t - D) + V_\delta \end{cases} \\
\xi_{t+1} &= -\sum_{s=1}^{S-1} \xi_{t-s} + V_\xi
\end{aligned}
\tag{1}
$$

where $V_y \sim N(0, \sigma_y^2)$, $V_\mu \sim N(0, \sigma_\mu^2)$, $V_\delta \sim N(0, \sigma_\delta^2)$, and $V_\xi \sim N(0, \sigma_\xi^2)$.

The data trend can be seen as a superimposition of a level μ_t and a slope δ_t. The latter is the expected increase in the level from time t to time $t+1$. The level μ_t may have a linear (local trend) or a nonlinear (semilocal trend) expression. The

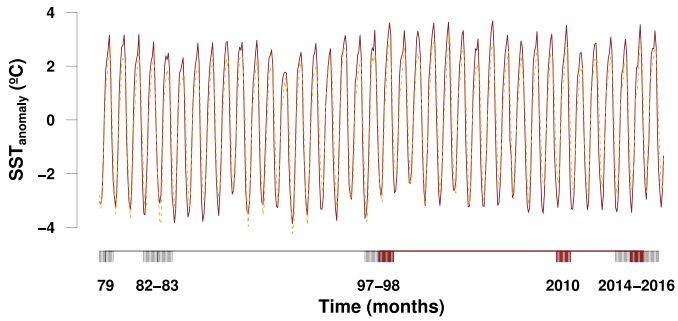

Fig. 5. Time series of SSTA. Plotted are curves for South Red Sea (lined dark red), Central Red Sea (dashed orange), and North Red Sea (dotted grey). Grey ticks are used to indicate El Niño years, whereas red ticks are used to denote bleaching events.

local trend is expressed as a random walk. A semilocal trend is a hybrid model that modifies the local trend model by adding to the level a slope written as an autoregressive (AR(1)) process $D + \rho(\delta_t - D)$, where D is the long-term slope of the trend, δ_t is the short-term autoregressive deviation from the long-term trend and the parameter $\rho\,(|\rho| < 1)$ plays a memory role, leading to long deviations from D if its value is close to 1. If the errors are assumed to follow a student's t-distribution, the local trend model is named in this case a T-local model. The latter is usually used for its adequacy to capture dramatic changes in the data, which makes the model robust against outliers and/or shifts in the slope [52].

The seasonal component is expressed as the total value of a nonfull ranked sum $(< S)$ of a variable ξ_t representing the joint contribution of the seasons to y_t. The mean of ξ_{t+1} is such as the total effect is zero when summed over the total number of seasons $S = 12$. This quantity is subtracted at each time from the trend of the monthly mean SSTA time series.

The regression component $(\beta^T \mathbf{x}_t)$ incorporates the predictors and their lag by shifting the corresponding predictors in time. In our case, $\mathbf{x}_t$ includes 7 climate indices with a total of 16 predictors (the MJO index has 10 components representing its phases) and all their time-shifted series. Therefore, the number of potential regressors in our model is large (171 predictors) and the design matrix $\mathbf{X}$ including all predictors for every time step is a (444×171) matrix.

In the BSTS model, the parameters are inferred based on the observational data under prior specifications. This framework combines three approaches to estimate the unknown parameters as well as to perform future predictions, which as follows:

1) a Kalman filter [31], [53] to estimate the structural model trend (level, slope and parameters of the slope if included) and seasonality;
2) a spike and slab regression [54] for regressor selection and regression coefficients estimation; and
3) a Bayesian model averaging [55] of multiple predictions with the selected model.

Here, we summarize the model calibration (parameter estimation) and prediction steps. The reader is referred to Scott and Varian [52] for more details. In the following, we denote

by θ the set of model parameters and by $\boldsymbol{\alpha} = (\alpha_1, \ldots, \alpha_n)$ the latent space containing all state components for n time steps. The vector α_i contains concatenated state components. The observation vector is given by $\mathbf{y} = \{y_1, \ldots, y_t\}$.

1) Regression Parameters Specifications: Future SST over a given clustered region is predicted by incorporating information from historical values of the SST time series, the time series of the climate indices and their shifted time series ($1-9$ months lag of SST and climate indices). Including past behavior contributes to enlarging the number of potential predictors in the regression model. When encountering a large number of predictors, a factor selection for regressors is needed. This consists in an *a priori* selection of a subset of potential predictors so that the regression has a sparse matrix. The idea consists in inducing sparsity by placing a spike and slab prior distribution on the regression coefficients [54], [55]. The spike and slab regression forces many regression coefficients to be exactly equal to zero when sampling from the posterior distribution of the regression model [56].

By assuming the spike and slab prior, an additional parameter is included in the model for the purpose of regressor selection. The inclusion of a particular regressor is thus ensured by a parameter γ, of the same length as β, that $\gamma_i = 1 \Rightarrow \beta_i \neq 0$ and $\gamma_i = 0 \Rightarrow \beta_i = 0$.

The functional form of the spike part is assumed to follow a Bernoulli distribution so that $p(\gamma) = \prod_i \kappa_i^{\gamma_i}(1-\kappa_i)^{1-\gamma_i}$ for all regressions. A common prior inclusion probability is elicited from the expected number of nonzero coefficients k out of K coefficients so that $\kappa = \frac{k}{K}$. The latter is assumed to be fixed and to be the same to all regressors under noninformative prior.

The slab component is used for the prior value of the nonzero coefficients. It is common to assume Zellner's g-prior [57] to express the conditionally conjugacy of the slab prior given the fact that the latter is conditional on the prior knowledge on κ. It is given by

$$\beta_\gamma | \gamma, \sigma_\varepsilon^2 \sim \mathcal{N}\left(b_\gamma, \sigma_\varepsilon^2 \left(\Omega_\gamma^{-1}\right)^{-1}\right) \tag{2}$$

where b_γ is a prior guess of the regression coefficient assumed to be zero except for the intercept, and a prior precision of the nonzero coefficient ($\gamma_i = 1$) being $\Omega_\gamma^{-1} = \kappa(\mathbf{X}^{\mathrm{T}}\mathbf{X})/n$. The latter expresses the average information in κ regressions. The prior of σ_ε^{-2} is given by $\Gamma(\frac{df}{2}, \frac{ss}{2})$, where df and ss can be elicited by the prior belief of the modeler. Often, $ss = df(1-R^2)\sigma_y^2$ where df is the number of the observations and R^2 set to an expected value in $[0, 1]$.

2) Parameter Calibration: An MCMC technique is used here to sample the posterior distribution of the model parameters $\theta = (\beta, \sigma_y^{-2}, \gamma)$ given by $p(\theta, \boldsymbol{\alpha}|\mathbf{y})$. A Gibbs sampler is applied, by alternating draws of $p(\boldsymbol{\alpha}|\theta, \mathbf{y})$ (data augmentation step) and $p(\theta|\boldsymbol{\alpha}, \mathbf{y})$ (parameter–simulation step), which produces a chain of sequences $(\theta, \boldsymbol{\alpha})_j$ (j in N samples).

a) Estimate of $p(\boldsymbol{\alpha}|\theta, \mathbf{y})$ and the Kalman filter: The fast mean smoothing method of Durbin and Koopman [58] is used, which estimates the variance of $p(\boldsymbol{\alpha}|\theta, \mathbf{y})$ and the corresponding expectations using the Kalman filter. The idea is to simulate from the system (1) a set of $(\mathbf{y}^*, \boldsymbol{\alpha}^*) \sim p(\mathbf{y}, \boldsymbol{\alpha}|\theta)$. The fast smoother is then used to subtract the conditional mean $E(\boldsymbol{\alpha}^*|\theta, \mathbf{y}^*)$ to obtain a zero mean noise and get the correct variance [56], and then to add the estimated conditional mean $E(\boldsymbol{\alpha}|\theta, \mathbf{y})$. The latter allows to sample $\boldsymbol{\alpha}$ with an adequate distribution $p(\boldsymbol{\alpha}|\theta, \mathbf{y})$.

All state components depend on variance parameters expressed in the error terms. The prior of variances follow a Gamma distribution $\Gamma(10^{-2}, 10^{-2}\sigma_y^2)$ where $\sigma_y^2 = \frac{1}{n-1}\sum_t (y_t - \bar{y})^2$. Thanks to the conjugacy, the posterior distribution will remain Gamma distributed.

The variances in the error terms relative to the state components are estimated by sampling their full conditional distributions. Here, we illustrate it for the trend and the slope components. Their full conditional distribution is given by the multiplication of their individual Gamma distributions so that

$$p\left(\sigma_\mu^2, \sigma_\delta^2 | \boldsymbol{\alpha}\right) = \Gamma\left(\frac{\mathrm{df}_\mu + \mathrm{n} - 1}{2}, \frac{\mathrm{V}_\mu}{2}\right) \Gamma\left(\frac{\mathrm{df}_\delta + \mathrm{n} - 1}{2}, \frac{\mathrm{V}_\delta}{2}\right) \tag{3}$$

where df_μ and df_δ are the number of observations used in estimating V_μ and V_δ, respectively. The latter are estimated using the observational data directly in the corresponding equations in (1).

b) Estimate of $p(\theta|\boldsymbol{\alpha}, \mathbf{y})$: Conditional on $\boldsymbol{\alpha}$, the time series $\mathbf{y} = \{y_1, \ldots, y_t\}$ are independent from the regression component [58], i.e., the full conditional distribution for (β, σ_y^{-2}) is independent from the other state components, resulting in independent draws from $p(\theta|\boldsymbol{\alpha}, \mathbf{y})$. The conditional posteriors for the regression coefficient and the variance σ_y^{-2} can be found in Gelman *et al.* [59]. They are given by normal and inverse Gamma distributions, respectively

$$p\left(\beta | \mathbf{y}, \boldsymbol{\alpha}, \gamma, \sigma_y^{-2}\right) = \mathcal{N}\left(\tilde{\beta}_\gamma, \sigma_y^2 V_\gamma\right) \tag{4}$$

and

$$p\left(\sigma_y^{-2} | \mathbf{y}, \boldsymbol{\alpha}, \gamma\right) = \Gamma\left(\tfrac{df+n}{2}, ss + \tilde{S}\right) \tag{5}$$

where

$V_\gamma^{-1} = \mathbf{X}^T\mathbf{X} + \Omega_\gamma^{-1}$, $\tilde{\beta}_\gamma = V_\gamma(\mathbf{X}^T\tilde{\mathbf{y}}_\gamma + \Omega_\gamma^{-1}b_\gamma)$, $\tilde{S} = \sum_{t=1}^n (\tilde{y}_\gamma - \mathbf{x}_t^T\beta_\gamma^T)^2 + (\tilde{\beta}_\gamma - b_\gamma)^T\Omega_\gamma^{-1}(\tilde{\beta}_\gamma - b_\gamma)$.

The inclusion probability $p(\gamma|\boldsymbol{\alpha}, \mathbf{y})$ assigned to the different regression coefficient are updated using the data and its distribution is given by

$$p\left(\gamma | \mathbf{y}, \boldsymbol{\alpha}\right) \propto \frac{\left|\Omega^{-1}\right|^{-1/2}}{\left|V_\gamma^{-1}\right|^{-1/2}} \tilde{S}^{-(df+n)/2}. \tag{6}$$

3) Computation and Future Predictions: Denote $\varphi = (\boldsymbol{\alpha}, \beta, \sigma_y^{-2}, \gamma)$. We seek to estimate the posterior distribution $p(\varphi|\mathbf{y})$ by sampling a set of φ_j for j in N using a Markov chain. These φ_j's are estimated by the following procedures.

1) Sampling the latent space $\boldsymbol{\alpha}$ from $p(\boldsymbol{\alpha}|\theta, \mathbf{y})$ using the approach of Durbin and Koopman [58].
2) Sampling from $p(\gamma|\boldsymbol{\alpha}, \mathbf{y})$ given by (6) using a Gibbs sampler.
3) Sampling from $p(\beta, \sigma_y^{-2}|\boldsymbol{\alpha}, \mathbf{y})$ given by the product of the conditional posteriors for the regression coefficient and the variance specified in (4) and (5), respectively, using a Gibbs sampler.

TABLE V
DIAGNOSTIC VALIDATION ESTIMATES OF CALIBRATED MODELS USING LOCAL, SEMILOCAL, AND *T*LOCAL TRENDS

Model	Region	residual sd	prediction. sd	R^2
Local	**1**	0.270	0.460	0.987
	2	0.237	0.412	0.985
	3	0.382	0.508	0.975
Semi-local	**1**	0.237	0.430	0.989
	2	0.215	0.387	0.988
	3	0.308	0.507	0.983
T-local	**1**	0.19	0.517	0.99
	2	0.145	0.503	0.995
	3	0.380	0.508	0.975

Note: *residual.sd* is the posterior mean of the residual standard deviation parameter, *prediction.sd* is the standard deviation of the one-step-ahead prediction errors for the training data, and R^2 gives the proportion by which the residual variance is less than the variance of the original observations. Note that standard deviations of the original times series are 2.351, 1.99, and 2.404 for regions 1, 2, and 3, respectively.

A sequence of sampled hyperparameters φ drawn from $p(\varphi|\mathbf{y})$ is used to estimate the predictive distribution $p(\tilde{y}|\varphi)$ of a future (unknown) $\tilde{y}$ after averaging

$$p\left(\tilde{y}|\mathbf{y}\right) = \int p\left(\tilde{y}|\varphi\right) p\left(\varphi|\mathbf{y}\right) p\left(\varphi\right) \tag{7}$$

namely by iterating the equations in (1) given the corresponding parameters drawn in φ. Note that the Monte Carlo samples from the posterior predictive distribution take into account the sparsity of the model as many regression coefficients will be equal to zero. The prediction value is given by the expected value $E(\tilde{y}|\mathbf{y})$ of the sample drawn from the posterior predictive distribution, and uncertainty is expressed by the sample variance $V(\tilde{y}|\mathbf{y})$.

IV. RESULTS

A. Model Selection, Verification, and Validation

We calibrated different BSTS models depending on prior specifications, using a training dataset starting from the beginning of the time series (January 1979) up to time $t = 396$ (December 2012). The prediction period for model verification and validation (V&V) lasts 4 years (48 time points).

Each BSTS model includes a trend, a seasonal component ($S = 12$), and a regression component in the state equation. Regressors are included in the structural time series model in a static framework where the regression coefficients are fixed. The unknown coefficients and model parameters of the structural model are estimated by first assigning priors on each of them and then sampling from the posterior distribution using MCMC as stated in the methodology. The samples from the posterior distribution for the parameters are then used to construct a posterior distribution for the time series predictions.

The validity of the three calibrated models with a local, a semilocal, and a *T*-local trends, to adequately represent the data, is verified using the residual standard deviation comparison (see Table V). All models are valid judging by the magnitude of the residuals compared to the sample standard deviation. The latter constitutes a test of how close is the fit to the data; the smaller the residual standard deviation, the more adequate is the model to represent the data.

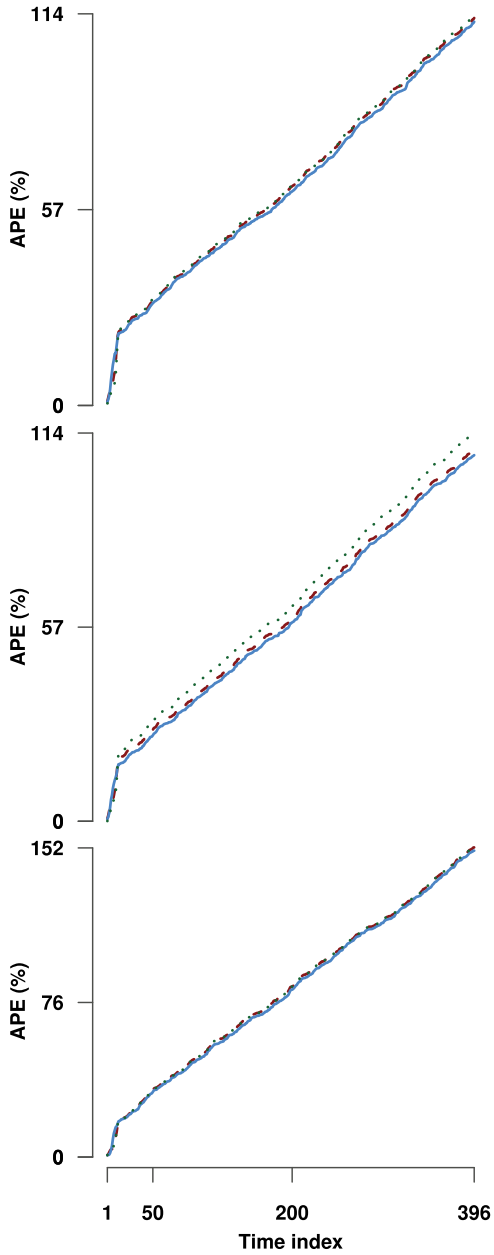

Fig. 6. Time evolution of the cumulative relative errors in percentage of the one-step ahead prediction. Shown are plots for regions 1–3, arranged from top to bottom. Each plot shows curves obtained using the semilocal trend (lined blue), the local trend (dashed red), and the *T*-local trend (dotted green)-based models.

By comparing the accumulative forward prediction error (APE) (one step prediction ahead) of each model (see Fig. 6), the semilocal trend-based model, which has lower values over all clustered regions, is selected and used henceforward. Note that the rationale for using APE as a data-driven method for model selection is discussed in Wagenmakers *et al.* [60].

A verification test of the model predictability consists of comparing a one-left out observation data to the predicted data as resulting from the BSTS model. The time series being ordered,

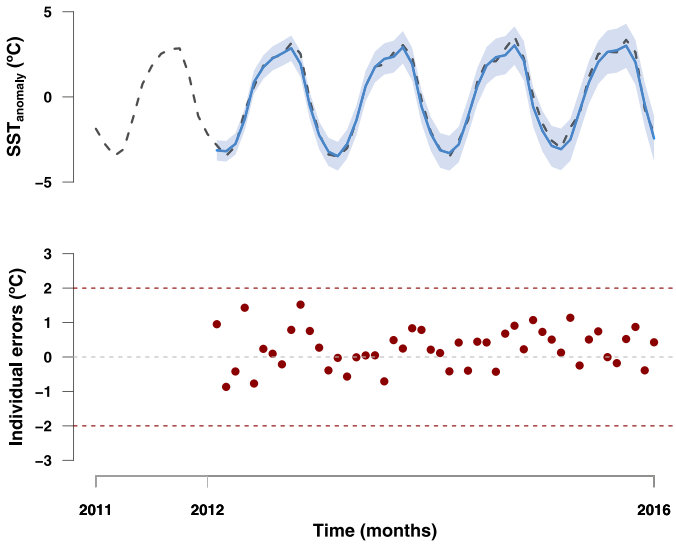

Fig. 7. Top: Time series of the long-term prediction of the monthly SSTA over Region 3 using the semilocal trend-based model. The filled (blue) area represents 95% confidence interval. Bottom: Individual errors versus time. The dashed horizontal lines (red) corresponds to 2σ interval bounds.

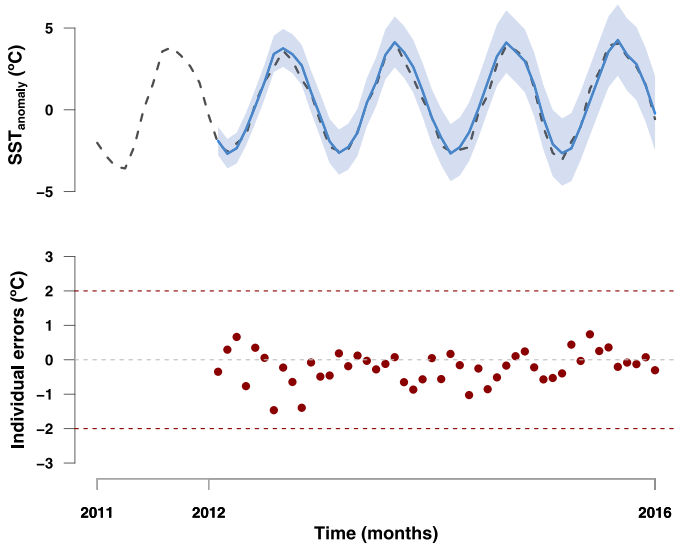

Fig. 9. Top: Time series of the long-term prediction of the monthly SSTA over Region 3 using the semi-local trend-based model. The filled (blue) area represents 95% confidence interval. Bottom: Individual errors versus time. The dashed horizontal lines (red) corresponds to 2σ interval bounds.

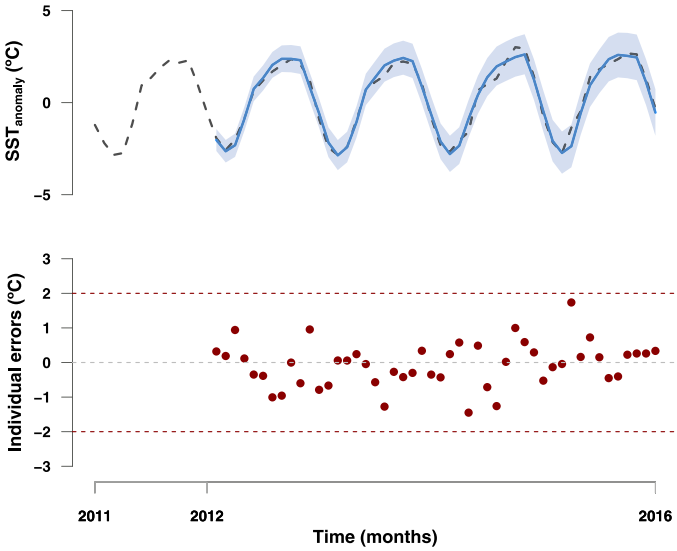

Fig. 8. Top: Time series of the long-term prediction of the monthly SSTA over Region 3 using the semilocal trend-based model. The filled (blue) area represents 95% confidence interval. Bottom: Individual errors versus time. The dashed horizontal lines (red) corresponds to 2σ interval bounds.

TABLE VI
ESTIMATES OF THE CALIBRATION ADEQUACY FOR THE SEMILOCAL TREND-BASED MODEL

Region	sd.original.series	residual.sd	prediction.sd	R^2
1	2.324	0.235	0.406	0.99
2	1.953	0.163	0.382	0.993
3	2.401	0.326	0.497	0.982

every one-time point is predicted with the model calibrated on the remaining dataset (prior to the prediction set).

The long-term predictions using the selected semi-local-based model are accurate when comparing the observed SSTA with the predicted expected means. All predictions lie inside the 95% credible interval (filled blue area around the expected mean in top panels of Figs. 7, 8, and 9 for regions 1, 2, and 3, respectively).

The predictability of the selected model, semilocal BSTS model, assessed by the standardized individual predictive error, is satisfactory and the model is reliable as more than 95% of errors remain within the 2σ intervals (bottom panels of Figs. 7, 8, and 9 for regions 1, 2, and 3, respectively).

The analysis below is performed using a semilocal-based BSTS model, calibrated and validated (see Table VI) using the observational time series from January 1979 to April 2017 of the different specified data. For each clustered region, the SSTA data over the prediction period (May 2017–September 2018) have been processed first by estimating their anomaly on the basis of the mean over the calibration period, and second by determining the cluster to witch each time series belongs based on Ward' s minimum variance criterion, as stated in Section II.

B. Factor Selection per Region

Predictors of SSTA per region are selected if their posterior inclusion probabilities are greater than 0.1. They are represented in violin plots in Fig. 10 (left-hand side panel). 10% of the total 5.10^4—MCMC runs were discarded as burn runs.

The red dot represents the median, the thick grey bar in the center represents the interquartile range, and the thin grey line represents the 95% confidence interval. On each side of the grey line is a kernel density estimate to show the distribution shape of the data in light pink. In the wider sections, members of the population have the higher probability to have a given value, the opposite is for narrower sections.

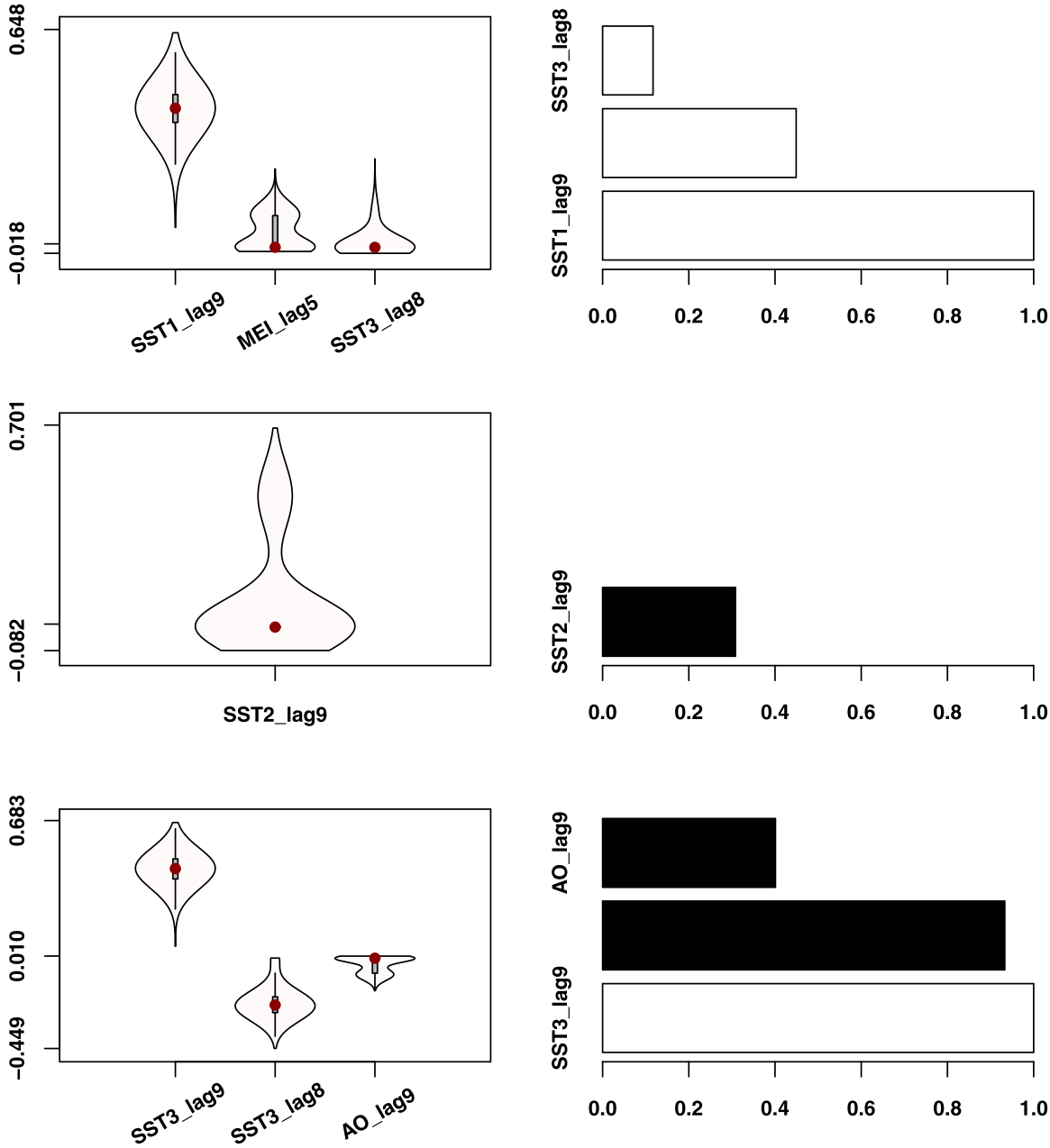

Fig. 10. Left panels: Violin plot of selected factors from Regions 1–3, arranged from top to bottom. Factors with inclusion probability ≥ 0.1 are specifically selected. Violin plots include a marker for the median of the data and a box indicating the interquartile range. Right panels: Bar plots of the posterior inclusion probabilities for the most likely predictors in the regression for Regions 1–3. White bars correspond to positive coefficients and black bars to negative coefficients.

The signed contribution of each factor per region to SST variability is summarized in bar plots of Fig. 10 (right-hand side panel), summarized in Table VII and explained in the following.

The analysis enables us to show, in a systematic and reliable fashion, that among the seven climate indices considered, MEI–ENSO and AO have the most important impact on the SST variability of the Red Sea, which when combined with the respective lagged SSTA (either 8 or 9 months) per region, constitute the most important predictors of future SSTA. The 8 or 9 months lagged SSTA contribute positively to variations of SSTA, except over the central region (Region 2).

TABLE VII
SUMMARY OF THE INCLUSION PROBABILITY (INC.PROB) IN THE BSTS MODEL, MEAN, AND STANDARD DEVIATION OF THE MAIN SELECTED FACTORS PER CLUSTERED

	Selected factors			mean	sd	inc. prob
	Variable	Region	Time lag			
Region 1	SST	1	9	0.413	0.088	0.980
	ENSO	-	5	0.034	0.050	0.335
	SST	3	8	0.012	0.034	0.123
Region 2	SST	2	9	0.461	0.065	1
Region 3	SST	3	9	0.449	0.074	1
	SST	3	8	-0.222	0.077	0.941
	AO	-	9	-0.027	0.040	0.334

MEI–ENSO index lagged by 5 months contributes positively to variations of SSTA over Region 1. Note that predictions of SSTA over Region 1 are not only based on past memories of its local region but also SSTA values of Region 3 lagged with 8 months.

The three MJO modes at 70°E, 80°E, and 120°W (not included in this study) have inclusion probability greater than 0.05, whereas all remaining indices have low inclusion probability. If the inclusion probability was reduced to 0.05, the three MJO modes at 70°E, 80°E, and 120°W may appear in the probable predictors of SST over the Southern part of the Red Sea (Region 1). Their possible contributing effect on SST variations over this region is probably linked to ENSO, through their impact on the atmospheric circulation and surface temperature around the subtropics. This can contribute to the speed of development and intensity of ENSO episodes.

SSTA over Region 2 is mainly predicted using its 9-month-lagged value where the past has a positive impact on future predictions. This region could be a transition region for SST exchanges between the northern and southern Red Sea, where the indices have a direct lagged effect on the latter [26].

Our study shows that AO index lagged by 9 months is an important predictor of SSTA over the northern Red Sea. It affects negatively variations of SSTA over this region. It is known that AO is the leading mode in the Northern Hemisphere winter circulation pattern. This pattern is well documented in the winter time series of a coral record from the Northern Red Sea [61].

NAO is not an important predictor of SSTA over the northern region, but NAO variability was shown to be highly correlated with patterns of winter SST in the Red Sea [47], [62], [63]. The NAO strongly affects the ocean through latent and sensible heat exchanges [64] and it affects the Middle Eastern climate by inducing changes in the Atlantic westerly heat/moisture transport and Atlantic/Mediterranean SST [65]. Based on coral paleo records for the Central Red Sea, Rimbu *et al.* [66], [67] hypothesized that during winter, AO/NAO control this connection.

C. SSTA Predictions

To evaluate the predictability of the BSTS model calibrated with the training dataset (January 1979–April 2017) and the selected predictors, we predict SSTA for the following 22 months, till February 2019. The predicted SSTA per region is plotted in Fig. 11.

Note that for the design of the predictive data matrix, zeros were assigned to all predictors except for the important ones selected during the calibration step.

The comparison between the observations and predictions is conducted over all the prediction period up to September 2018. Observational monthly SSTs for the following months after April 2017 were retrieved from the same source as for the historical data. They are represented by dashed grey lines in Fig. 11.

Prediction errors, calculated as the differences between the predicted and observational SST over each clustered region, all fall in average below 0.5 °C (see Table VIII). Moreover, the predictions lay within the 95% confidence interval (see shaded grey area in Fig. 11), supporting the predictive ability of the model.

For the remaining 5 months, from October 2018 up to February 2019 (plotted in dark red in Fig. 11), no data are available for validation. The predictions are compared to the observational data distribution to test their significance for each month, *inprimis* the $(\min, \max)$ interval and mean of the data (plotted in green segments). Recall that the choice of the 5 months is justified by the minimum time lag shared between the selected predictors. Thus, future predictions are possible for a time laps of a maximum of 5 months ahead of the available observational data for the whole Red Sea.

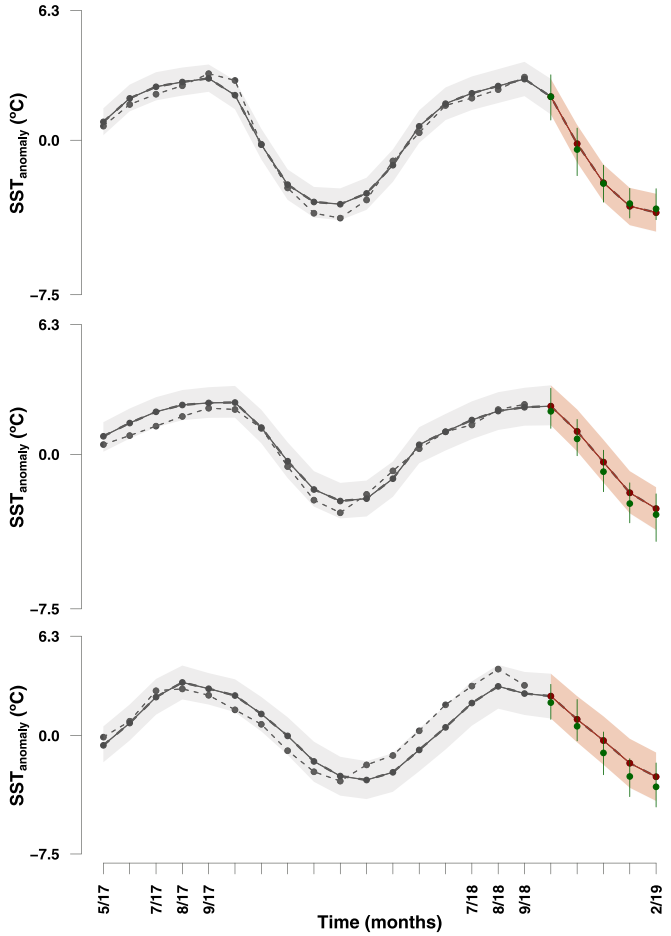

Fig. 11. Predicted SSTA for five seasons for Regions 1–3, arranged from top. The filled area represents the 95% confidence interval. The prediction cover the period from May 2017 to February 2019. Quantiles of observational SSTA for each month are superimposed in green.

TABLE VIII
SUMMARY STATISTICS OF THE PREDICTION ERRORS PER REGION

Region	min	Q1	median	Q2	max
1	-0.676	-0.312	-0.181	0.018	0.717
2	-1.227	-0.764	-0.419	0.409	1.562
3	-1.120	-0.370	0.219	0.725	1.582

Note: $Q1$ and $Q2$ are the main quantiles.

V. Conclusion

In this study, we explored the predictive ability of Red Sea surface temperature to climate indices variations, and more specifically, the seasonal predictability. We also investigated the most important predictive factors of SST, and the corresponding time delays, which may drive climate predictions.

The predictability of the SST in the Red Sea is assessed using both global climate indices and local SST conditions, using a structural time series model over three main regions, clustered-based on long-term variability dissimilarities. The model was calibrated following a Bayesian perspective to account for uncertainty in the different parameters and in the predictions.

The structural time series model is a powerful predictive tool, being modular and flexible. Systematically and efficiently selecting which components to include in the model structure makes it more reliable and interpretable, and in addition, prevents overfitting [68]. The semilocal trend-based model with a preserved past memory is found to be the most suitable for our application.

Efficiency in the prediction approach proposed here is enforced by avoiding redundancy and predicting over the clustered regions of the Red Sea, and by selecting a small set of the most important predictors at the same time as model training using a Bayesian paradigm and an MCMC algorithm with a structural time series model.

The new insights gained from applying this approach are that large-scale spatial patterns of ENSO (and at some extend MJO) are an important predictive factor over the southern Red Sea, whereas AO is a predictor of monthly SSTA over the Northern Red Sea. SST over the central region of the Red sea may be predicted based on its past memory only (9 months earlier). We also showed that a time lag of 8–9 months is an important lag for predictors of monthly SST. Moreover, our future predictions are reliable 5 months ahead.

Our findings are further supported by long coral record over the Northern Red Sea [61]. This record provides evidence that interaction between tropical and extratropical modes of the global climate system has an important control on the Middle East climate variability on interannual longer time-scales since at least 1750.

References

[1] E. Osman *et al.*, "Thermal refugia against coral bleaching throughout the northern red sea," *Global Change Biol.*, vol. 24, no. 2, pp. e474–e484, 2018.

[2] T. P. Hughes *et al.*, "Global warming and recurrent mass bleaching of corals," *Nature*, vol. 543, pp. 373–377, 2017.

[3] T. Hughes *et al.*, "Spatial and temporal patterns of mass bleaching of corals in the Anthropocene," *Science*, vol. 359, no. 6371, pp. 80–83, 2018.

[4] N. Cantin, A. Cohen, K. Karnauskas, A. Tarrant, and D. McCorkle, "Ocean warming slows coral growth in the central red sea," *Science*, vol. 329, no. 5989, pp. 322–325, 2010.

[5] Y. Abualnaja, V. Papadopoulos, S. Josey, I. Hoteit, H. Kontoyiannis, and D. Raitsos, "Impacts of climate modes on air–sea heat exchange in the Red Sea," *J. Climate*, vol. 28, pp. 2665–2681, 2015.

[6] A. Chakraborty, S. Behera, M. Mujumdar, R. Ohba, and T. Yamagata, "Diagnosis of tropospheric moisture over Saudi Arabia and influences of IOD and ENSO," *Monthly Weather Rev.*, vol. 134, pp. 598–617, 2006.

[7] E. Tyrlis, J. Lelieveld, and B. Steil, "The summer circulation in the eastern Mediterranean and the Middle East: Influence of the South Asian monsoon," *Climate Dyn.*, vol. 40, pp. 1103–1123, 2013.

[8] D. Rizou, H. Flocas, P. Athanasiadis, and A. Bartzokas, "Relationship between the Indian summer monsoon and the large-scale circulation variability over the Mediterranean," *Atmos. Res.*, vol. 152, pp. 159–169, 2015.

[9] M. Barlow, M. Wheeler, B. Lyon, and H. Cullen, "Modulation of daily precipitation over southwest Asia by the Madden-Julian oscillation," *Monthly Weather Rev.*, vol. 133, pp. 3579–3594, 2005.

[10] R. Attada, R. Yadav, R. Kunchala, H. Dasari, O. Knio, and I. Hoteit, "Prominent mode of summer surface air temperature variability and associated circulation anomalies over the Arabian Peninsula," *Atmos. Sci. Lett.*, vol. 19, 2018, Art. no. e860.

[11] Č. Branković and T. N. Palmer, "Seasonal skill and predictability of ECMWF PROVOST ensembles," *Quart. J. Roy. Meteorol. Soc.*, vol. 126, no. 567, pp. 2035–2067, 2000.

[12] A. Weisheimer and T. N. Palmer, "On the reliability of seasonal climate forecasts," *J. Roy. Soc. Interface*, vol. 11, no. 96, 2014, Art. no. 20131162.

[13] A. Barnston, M. Tippett, H. van den Dool, and D. Unger, "Toward an improved multimodel ENSO prediction," *J. Appl. Meteorol. Climatol.*, vol. 54, no. 7, pp. 1579–1595, 2015.

[14] T. N. Stockdale, M. A. Balmaseda, and A. Vidard, "Tropical Atlantic SST prediction with coupled ocean–atmosphere GCMs," *J. Climate*, vol. 19, no. 23, pp. 6047–6061, 2006.

[15] T. Krishnamurti, A. Chakraborty, R. Krishnamurti, W. Dewar, and C. Clayson, "Seasonal prediction of sea surface temperature anomalies using a suite of 13 coupled atmosphere ocean models," *J. Climate*, vol. 19, no. 23, pp. 6069–6088, 2006.

[16] M. Hong, X. Chen, R. Zhang, D. Wang, S. Shen, and V. P. Singh, "Forecasting experiments of a dynamical statistical model of the sea surface temperature anomaly field based on the improved self memorization principle," *Ocean Sci.*, vol. 14, pp. 301–320, 2018.

[17] A. G. Barnston and T. M. Smith, "Specification and prediction of global surface temperature and precipitation from global SST using CCA," *J. Climate*, vol. 9, no. 11, pp. 2660–2697, 1996.

[18] A. Saunders, M. Ghil, and D. Neelin, "Forecasts of Nino-3 SST anomalies and SOI based on singular spectrum analysis combined with the maximum entropy method," *Exp. Long-Lead Forecast Bull.*, vol. 6, no. 3, pp. 43–44, 2001.

[19] B. Tang, W. W. Hsieh, A. H. Monahan, and F. T. Tangang, "Skill comparisons between neural networks and canonical correlation analysis in predicting the equatorial pacific sea surface temperatures," *J. Climate*, vol. 13, no. 1, pp. 287–293, 2000.

[20] S. J. Mason and G. M. Mimmack, "Comparison of some statistical methods of probabilistic forecasting of ENSO," *J. Climate*, vol. 15, no. 1, pp. 8–29, 2002.

[21] Z. T. Segele, P. J. Lamb, and L. M. Leslie, "Large-scale atmospheric circulation and global sea surface temperature associations with Horn of Africa June–September rainfall," *Int. J. Climatol.*, vol. 29, no. 8, pp. 1075–1100, 2009.

[22] A. Hoell and C. Funk, "The ENSO-related West Pacific sea surface temperature gradient," *J. Climate*, vol. 26, pp. 9545–9562, 2013.

[23] N. Zhang, M. Feng, H. Hendon, A. Hobday, and J. Zinke, "Opposite polarities of ENSO drive distinct patterns of coral bleaching potentials in the southeast Indian Ocean," *Sci. Rep.*, vol. 7, 2017, Art. no. 2443.

[24] H. Dasari, S. Langodan, Y. Viswanadhapalli, B. Vadlamudi, V. Papadopoulos, and I. Hoteit, "ENSO influence on the interannual variability of the Red Sea convergence zone and associated rainfall," *Int. J. Climatol.*, vol. 38, pp. 761–775, 2018.

[25] K. B. Karnauskas and B. H. Jones, "The interannual variability of sea surface temperature in the red sea from 35 years of satellite and in situ observations," *J. Geophys. Res.: Oceans*, vol. 123, no. 8, pp. 5824–5841, 2018.

[26] G. Krokos, V. P. Papadopoulos, S. S. Sofianos, H. Ombao, P. Dybczak, and I. Hoteit, "Natural climate oscillations may counteract red sea warming over the coming decades," *Geophys. Res. Lett.*, vol. 46, no. 6, pp. 3454–3461, 2019.

[27] Y. Xue, A. Leetmaa, and M. Ji, "ENSO prediction with Markov models: The impact of sea level," *J. Climate*, vol. 13, no. 4, pp. 849–871, 2000.

[28] T. Kim, J.-Y. Shin, H. Kim, S. Kim, and J.-H. Heo, "The use of large-scale climate indices in monthly reservoir inflow forecasting and its application on time series and artificial intelligence models," *Water*, vol. 11, no. 2, 2019, Art. no. 374.

[29] D. Robertson and Q. Wang, "A Bayesian approach to predictor selection for seasonal streamflow forecasting," *J. Hydrometeorol.*, vol. 13, no. 1, pp. 155–171, 2012.

[30] A. Schepen, Q. Wang, and D. Robertson, "Evidence for using lagged climate indices to forecast Australian seasonal rainfall," *J. Climate*, vol. 25, no. 4, pp. 1230–1246, 2012.

[31] A. Harvey, *Forecasting, Structural Time Series Models and the Kalman Filter*. Cambridge, U.K.: Cambridge Univ. Press, 1990.

[32] J. Hamilton, *Time series analysis*. Princeton, NJ, USA: Princeton Univ. Press, 1994.

[33] P. Berrisford *et al.*, "The ERA-Interim archive," ERA Report Series 1, 2009. [Online]. Available: https://www.ecmwf.int/node/8173

[34] D. Dee *et al.*, "The ERA-Interim reanalysis: Configuration and performance of the data assimilation system," *Quart. J. Roy. Meteorol. Soc.*, vol. 137, pp. 553–597, 2011.

[35] C. Price, L. Stone, A. Huppert, B. Rajagopalan, and P. Alpert, "A possible link between El Niño and precipitation in Israel," *Geophys. Res. Lett.*, vol. 25, pp. 3963–3966, 1998.

[36] H. Athar, "Teleconnections and variability in observed rainfall over Saudi Arabia during 1978–2010," *Atmos. Sci. Lett.*, vol. 16, pp. 373–379, 2015.

[37] D. Thompson and J. Wallace, "The Arctic oscillation signature in the wintertime geopotential height and temperature fields," *Geophys. Res. Lett.*, vol. 25, pp. 1297–1300, 1998.

[38] A. Barnston and R. L. RE, "Classification, seasonality, and persistence of low-frequency atmospheric circulation patterns," *Monthly Weather. Rev.*, vol. 115, pp. 1083–1126, 1987.

[39] G. Walker, "Correlation of seasonal variations in weather IX: A further study of world weather," *Memoirs India Meteorol. Dept.*, vol. 24, pp. 275–332, 1925.

[40] N. Saji and T. Yamagata, "Possible impacts of Indian Ocean dipole mode events on global climate," *Climate Res.*, vol. 25, pp. 151–169, 2003.

[41] F. Pourasghar, T. Tozuka, H. Ghaemi, P. Oettli, S. Jananbakhsh, and T. Yamagata, "Influences of the MJO on intraseasonal rainfall variability over southern Iran," *Atmos. Sci. Lett.*, vol. 16, pp. 110–118, 2015.

[42] R. Washington, A. Hodson, E. Isaksson, and O. Macdonald, "Northern hemisphere teleconnection indices and the mass balance of Svalbard glaciers," *Int. J. Climatol.*, vol. 20, pp. 473–487, 2000.

[43] X. Wang, C. Wang, W. Zhou, D. Wang, and J. Song, "Teleconnected influence of North Atlantic sea surface temperature on the El Niño onset," *Climate Dyn.*, vol. 37, pp. 663–676, 2011.

[44] Y. Zhang, J. Wallace, and D. Battisti, "ENSO-like interdecadal variability: 1900-93," *J. Climate*, vol. 10, pp. 1004–1020, 1997.

[45] J. Chowdary, A. Parekh, C. Gnanaseelan, and P. Sreenivas,"Inter-decadal modulation of ENSO teleconnections to the Indian Ocean in a coupled model: Special emphasis on decay phase of El Niño," *Global Planet. Change*, vol. 112, pp. 33–40, 2014.

[46] H. Hasanean and M. Almazroui, "Teleconnections of the tropical sea surface temperatures to the surface air temperature over Saudi Arabia in summer season," *Int. J. Climatol.*, vol. 37, pp. 1040–1049, 2016.

[47] J. Hurrell, Y. Kushnir, G. Ottersen, and M. Visbeck, *The North Atlantic Oscillation: Climatic Significance and Environmental Impact* (Geophysical Monograph Series), vol. 134. Washington, DC, USA: Amer. Geophys. Union, 2003.

[48] C. Zhang and J. Gottschalck, "SST anomalies of ENSO and the Madden-Julian oscillation in the equatorial Pacific," *J. Climate*, vol. 15, pp. 2429–2445, 2002.

[49] D. Wilks, *Statistical Methods in the Atmospheric Sciences*, 3rd ed. Oxford, U.K.: Academic, 2011.

[50] J. Ward, "Hierarchical grouping to optimize an objective function," *J. Amer. Statist. Assoc.*, vol. 58, pp. 236–244, 1963.

[51] M. Charrad, N. Ghazzali, V. Boiteau, and A. Niknafs, "NbClust package for determining the best number of clusters," R package version 2.0.3, 2014. [Online]. Available: http://CRAN.R-project.org/package=NbClust

[52] S. Scott and H. Varian, "Predicting the present with Bayesian structural time series," *Int. J. Math. Model. Numer. Optim.*, vol. 5, pp. 4–23, 2014.

[53] R. Kalman, "A new approach to linear filtering and prediction problems," *ASME J. Basic Eng.*, vol. 82, pp. 35–45, 1960.

[54] E. George and R. McCulloch, "Approaches for Bayesian variable selection," *Statist. Sinica*, vol. 7, pp. 339–373, 1997.

[55] D. Madigan and A. Raftery, "Model selection and accounting for model uncertainty in graphical models using Occam's window," *J. Amer. Statist. Assoc.*, vol. 89, pp. 1535–1546, 1994.

[56] S. Scott and H. Varian, "Bayesian variable selection for nowcasting economic time series," in *Economic Analysis of the Digital Economy*. Chicago, IL, USA: Univ. Chicago Press, 2015, pp. 119–135.

[57] H. Chipman, E. George, and R. McCulloch, "The practical implementation of Bayesian model selection," in *Model Selection* (Lecture Notes–Monograph Series), vol. 38. P. Lahiri, Ed. Beachwood, OH, USA: Ins. Math. Statist., 2001, pp. 65–116.

[58] J. Durbin and S. Koopman, "A simple and efficient simulation smoother for state space time series analysis," *Biometrika*, vol. 89, pp. 603–615, 2002.

[59] A. Gelman, J. Carlin, H. Stern, D. Dunson, A. Vehtari, and D. Rubin, *Bayesian Data Analysis*. Boca Raton, FL, USA: CRC Press, 2013.

[60] E. Wagenmakers, P. Grünwald, and M. Steyvers, "Accumulative prediction error and the selection of time series models," *J. Math. Psychol.*, vol. 50, pp. 149–166, 2006.

[61] T. Felis, J. Pätzold, Y. Loya, F. Moaz, A. Nawar, and G. Wefer, "A coral oxygen isotope record from the northern Red Sea documenting NAO, ENSO, and North Pacific teleconnections on Middle East climate variability since the year 1750," *Paleoceanography*, vol. 15, pp. 679–694, 2000.

[62] M. Visbeck, J. Hurrell, L. Polvani, and H. Cullen, "The North Atlantic oscillation: Past, present, and future," *Proc. Nat. Acad. Sci. USA*, vol. 98, pp. 12876–12877, 2001.

[63] F. Yao and I. Hoteit, "Rapid Red Sea deep water renewals caused by volcanic eruptions and the North Atlantic Oscillation," *Sci. Adv.*, vol. 4, no. 6, 2018, Art. no. eaar5637.

[64] D. Cayan, "Latent and sensible heat flux anomalies over the northern oceans: Driving the sea surface temperature," *J. Phys. Oceanogr.*, vol. 22, pp. 859–881, 1992.

[65] H. Cullen and P. deMenocal, "North Atlantic influence on Tigris-Euphrates streamflow," *Int. J. Climatol.*, vol. 20, pp. 853–863, 2000.

[66] N. Rimbu, G. Lohmann, T. Felis, and J. Pätzold, "Arctic Oscillation signature in a Red Sea coral," *Geophys. Res. Lett.*, vol. 28, pp. 2959–2962, 2001.

[67] N. Rimbu, T. Felis, G. Lohmann, and J. Paatzold, "Winter and summer climate patterns in the European-Middle East during recent centuries as documented in a Northern Red Sea coral record," *Holocene*, vol. 16, pp. 321–330, 2006.

[68] K. Brodersen, F. Gallusser, J. Koehler, N. Remy, and S. Scott, "Inferring causal impact using Bayesian structural time-series models," *Ann. Appl. Statist.*, vol. 9, pp. 247–274, 2015.

[69] P. J. Rousseeuw, "Silhouettes: A graphical aid to the interpretation and validation of cluster analysis," *J. Computational Appl. Mathemat.*, vol. 20, pp. 53–65, 1987.

[70] T. Calinski and J. Harabasz, "A dendrite method for cluster analysis," *Commun. Statist.*, vol. 3, no. 1, pp. 1–27, 1974.

[71] J. A. Hartigan, *Clustering Algorithms*, 99th ed. Hoboken, NJ, USA: Wiley, 1975.

[72] L. J. Hubert and J. R. Levin, "A general statistical framework for assessing categorical clustering in free recall," *Psychol. Bull.*, vol. 6, no. 83, pp. 1072–1080, 1976.

[73] D. L. Davies and D. W. Bouldin, "A cluster separation measure," *IEEE Trans. Pattern Anal. Mach. Intell.*, vol. PAMI-1, no. 2, pp. 224–227, Apr. 1979.

[74] W. J. Krzanowski and Y. T. Lai, "A criterion for determining the number of groups in a data set using sum-of-squares clustering," *Biometrics*, vol. 44, no. 1, pp. 23–34, 1988.

[75] G. W. Milligan, "An examination of the effect of six types of error perturbation on fifteen clustering algorithms," *Psychometrika*, vol. 45, no. 3, pp. 325–342, 1980.

[76] G. W. Milligan, "A Monte Carlo study of thirty internal criterion measures for cluster analysis," *Psychometrika*, vol. 46, no. 2, pp. 187–199, 1981.

[77] R. Tibshirani, G. Walther, and T. Hastie, "Estimating the number of clusters in a data set via the gap statistic," *J. Roy. Statist. Soc.: Ser. B (Statist. Methodol.)*, vol. 63, no. 2, pp. 411–423, 2001.

[78] T. Frey and H. van Groenewoud, "A cluster analysis of the D2 matrix of white spruce stands in Saskatchewan based on the maximum minimum principle," *J. Ecology*, vol. 60, no. 3, pp. 873–886, 1972.

[79] F. J. Rohlf, "Methods of comparing classifications," *Annu. Rev. Ecology Systematics*, vol. 5, no. 1, pp. 101–113, 1974.

[80] J. C. Dunn, "Well separated clusters and optimal fuzzy partitions," *J. Cybern.*, vol. 4, no. 1, pp. 95–104, 1974.

[81] M. Halkidi, M. Vazirgiannis, and Y. Batistakis, "Quality scheme assessment in the clustering process," in *Principles of Data Mining and Knowledge Discovery*. Berlin, Germany: Springer, 2000, pp. 265–276.

[82] M. Halkidi and M. Vazirgiannis, "Clustering validity assessment: Finding the optimal partitioning of a data set," in *Proc. IEEE Int. Conf. Data Mining*, 2001, pp. 187–194.
[83] D. Ratkowsky and G. Lance, "Criterion for determining the number of groups in a classification," *Aust. Comput. J.*, vol. 3, no. 10, pp. 115–117, 1978.
[84] G. H. Ball and D. J. Hall, "Isodata, a novel method of data analysis and pattern classification," Stanford Res. Inst., Menlo Park, CA, USA, Tech. Rep. AD 699616, 1965.

Nabila Bounceur received the Dipl.Ing. degree in automatic from the National Polytechnic School, El Harrach, Algeria, in 2005, the M.Sc. degree in didactical teaching of mathematics from the University of Namur, Namur, Belgium, in 2008, and the Ph.D. degree in sciences from the University catholique de Louvain, Ottignies-Louvain-la-Neuve, Belgium, in 2015.

She is currently a Postdoctoral Fellow at the Uncertainty and Sensitivity Analysis group, Division of Computer, Electrical and Mathematical Science and Engineering, King Abdullah University of Science and Technology, Thuwal, Saudi Arabia, with Prof. O. Knio. In academia, she worked extensively on the application of statistical modeling approaches and analysis frameworks to understanding complex systems. She also collaborated with SWAN Insights Company in Belgium and gained an expertise in modeling and analysis of big data related systems. Her current research interests include statistical modeling and causality inference in climate and environmental applications.

Ibrahim Hoteit received the M.S. and Ph.D. degrees in applied mathematics from the University of Joseph Fourier, Grenoble, France, in 1998 and 2002, respectively.

He is currently a Professor in the earth sciences and engineering program at King Abdullah University of Science and Technology (KAUST), Thuwal, Saudi Arabia. He is also the Lead of the Virtual Red Sea Initiative, a joint initiative with Scripps Institution of Oceanography, MIT and Plymouth Marine Laboratory. He is also serving as the Associate Director of the Saudi Aramco Marine Environment Research Center, KAUST. He has coauthored more than 190 papers. His research interests include the modeling of oceanic and atmospheric systems on supercomputers and the analysis of their circulation and variability, with specific interest in data assimilation and inverse problems and associated uncertainty quantification for large-scale systems.

Dr. Hoteit was a corecipient of five Best Conference Paper Awards. He is serving as an Associate Editor for *PLOS One*, *Computational Geosciences*, *Mathematics of Climate and Weather Forecasting*, and *Atmospheric Science Letters*, and is a member of the American and European Geophysical Unions, the Society of Industrial and Applied Mathematics, and an elected member of the UNESCO Center of Pure and Applied Mathematics.

Omar Knio received the Ph.D. degree in mechanical engineering from the Massachusetts Institute of Technology (MIT), Cambridge, MA, USA, in 1990.

He held a Postdoctoral Associate position with MIT, before joining the Mechanical Engineering Faculty at Johns Hopkins University in 1991. In 2011, he joined the Mechanical Engineering and Materials Science Department at Duke University, where he also serves as Associate Director of the Center for Material Genomics. In 2012, he was named the Edmund T. Pratt, Jr., Professor of Mechanical Engineering and Materials Science at Duke. In 2013, he joined AMCS Program at King Abdullah University of Science and Technology, where he served as Deputy Director of the SRI Center for Uncertainty Quantification in Computational Science and Engineering.

Prof. Knio was the recipient of an Associated Western Universities Faculty Fellowship Award in 1996, a Friedrich Wilhelm Bessel Award in 2003, an R& D100 Award, in 2005, and a Distinguished Alumnus Award from the American University of Beirut, in 2005.